

Article

# Investigation of PZT Materials for Reliable Piezostack Deformable Mirror with Modular Design

Vladimir Toporovsky <sup>1,\*</sup>, Vadim Samarkin <sup>1</sup>, Alexis Kudryashov <sup>1,2</sup>, Ilya Galaktionov <sup>1</sup>, Alexander Panich <sup>3</sup> and Anatoliy Malykhin <sup>3</sup>

<sup>1</sup> Sadovsky Institute of Geosphere Dynamics, Russian Academy of Sciences, Leninskiy Pr. 38/1, Moscow 119334, Russia; samarkin@nighn.ru (V.S.); kud@activeoptics.ru (A.K.); galaktionov@activeoptics.ru (I.G.)

<sup>2</sup> Department of Physics, Moscow Polytechnic University, Bolshaya Semenovskaya Str. 38, Moscow 107023, Russia

<sup>3</sup> STCB 'Piezopribor', Institute for Advanced Technologies and Piezotechnics SFEDU, Milchakova Str. 10, Rostov-on-Don 344090, Russia

\* Correspondence: topor@activeoptics.ru; Tel.: +7-985-196-37-33

**Abstract:** This article presents a study of the electrophysical properties of a piezoceramic material for use in adaptive optics. The key characteristics that may be important for the manufacturing of piezoelectric deformable mirrors are the following: piezoelectric constants ( $d_{31}$ ,  $d_{33}$ ,  $d_{15}$ ), capacitance, elastic compliance values  $s$  for different crystal directions, and the dielectric loss tangent ( $\tan\delta$ ). Based on PZT ceramics, the PKP-12 material was developed with high values of the dielectric constant, piezoelectric modulus, and electromechanical coupling coefficients. The deformable mirror control elements are made from the resulting material—piezoceramic combs with five individual actuators in a row. In this case, the stroke of the actuator is in the range of 4.1–4.3 microns and the capacitance of the actuator is about 12 nF.

**Keywords:** adaptive optics; PZT materials; relaxor ferroelectrics; wavefront control; deformable mirrors; multilayer actuator



**Citation:** Toporovsky, V.; Samarkin, V.; Kudryashov, A.; Galaktionov, I.; Panich, A.; Malykhin, A.

Investigation of PZT Materials for Reliable Piezostack Deformable Mirror with Modular Design. *Micromachines* **2023**, *14*, 2004. <https://doi.org/10.3390/mi14112004>

Academic Editors: Weiqun Liu, Yipeng Wu and Jiawen Xu

Received: 18 August 2023

Revised: 19 October 2023

Accepted: 25 October 2023

Published: 28 October 2023



**Copyright:** © 2023 by the authors. Licensee MDPI, Basel, Switzerland. This article is an open access article distributed under the terms and conditions of the Creative Commons Attribution (CC BY) license (<https://creativecommons.org/licenses/by/4.0/>).

## 1. Introduction

Since the 1880s, studies of the properties of ferroelectrics have been carried out [1]. A special place in this series is occupied by piezoelectric ceramics, since such materials are capable of converting mechanical load into electrical energy and vice versa, and they could be used in various fields, such as smart sensing [2], energy harvesting [3], and as actuators for different applications [4,5]. The use of the piezoceramic devices as actuators can mainly be divided into three main areas: vibration suppressors [6], motors [7], and positioners [8]. The high reliability and positioning accuracy of such devices make it possible to use them in precision optical devices such as: fast steering mirrors [9,10], opto-mechanical adjustment systems (stepper motors [11], micro- and nanopositioning stages [12], etc. [13]), and piezoelectric wavefront correctors (bimorph [14–21], piezostack [22–31], etc. [32,33]) in various areas [34–45]. Considering the latter, it should be noted that piezomaterials manufactured for deformable mirrors [46–50] or tip-tilt stages [51] are subject to special requirements: high sensitivity to the applied voltages, reasonable stroke and blocking force, and the lowest possible electrical capacitance [52] to simplify the control electronics. The development of the multilayer stacks allowed for the generation of a large stroke at relatively low voltages (0...+120–300 V). Additional mechanisms can also be equipped to increase the displacement of the actuators to hundreds of microns: lever- [53], bridge- [54], and four-bar linkage [55] or Scott–Russell-type designs [56,57].

In the manufacturing of the piezoelectric deformable mirrors, solid solutions based on lead zirconate titanate (PZT) are used as a material for creating control elements due to their

high electrical properties (piezoceramic coefficients  $d_{31}$ ,  $d_{33}$ ), dielectric loss tangent, and blocking force [58–60]. Piezoceramic coefficients correspond to the deformable mirror stroke for compensation of the wavefront aberrations with the large amplitude. The dielectric loss tangent value impacts the ability of the wavefront corrector to mitigate influence of the aberrations dynamically changed with high speed. The blocking force parameter characterizes the maximum value of the force generated by a piezostack that is locked by a rigid, unyielding hold [61,62]. In addition, when creating piezostack deformable mirrors, a problem arises when increasing the spatial resolution of the control elements and, at the same time, obtaining a reliable design [63].

The paper is organized as follows. The Section 2 discusses the main parameters and properties of the piezomaterial for the manufacturing of the deformable mirror actuators. Based on such studies, piezoceramic modules were fabricated and their characteristics are discussed in Section 3. The conclusions are presented in Section 4.

## 2. Materials and Methods

### 2.1. Piezoelectric Effect and Material Properties

The piezoelectric effect could be explained by the property of the elementary cell of the material structure. In the elementary cell—the smallest symmetrical unit of material, from which, by repeating it many times, a microscopic crystal can be obtained—arises the non-symmetry of the center of the symmetry [64].

The elementary cell at temperatures above the critical one (Curie temperature [65]) has a cubic crystal lattice. If the temperature is below Curie temperature, then the elementary cell is distorted tetragonally towards one of the edges. As a result, the distances between positively and negatively charged ions also change (Figure 1). The displacement of ions from their original position leads to a separation of the centers of gravity of the charges within the cell, so that an electric dipole moment is formed. According to the energy conditions, the dipoles of neighboring elementary cells of the crystal are ordered by regions in the same direction, forming the so-called domains.

Mechanical compression or tension acting on a piezoelectric plate parallel to the direction of polarization leads to deformation of all elementary cells. In this case, the centers of gravity of the charges are mutually displaced inside the elementary cells, which are now predominantly parallel, and as a result, a charge is obtained on the surface.

The piezoelectric effect could be described in two main ways: direct and inverse phenomena. For sensing or harvesting applications, the piezoelectric material generates an electric signal under mechanical pressure that is expressed with an electrical displacement  $D$  of the material—this is the direct piezoelectric effect. At the same time, such materials could be exploited for actuation applications, however, it generates mechanical strain  $X$  under an applied electrical field—this is the inverse piezoelectric effect. The relationship between the direct and inverse effects is expressed as follows [66]:

$$\begin{cases} X = ST + dE \\ D = dT + \varepsilon E \end{cases}$$

where  $S$ —elastic compliance coefficient,  $T$ —stretching stress,  $d$ —piezoelectric coefficient,  $E$ —electric field, and  $\varepsilon$ —permittivity of the material.

Key parameters that could be considered significant in actuation applications of the piezomaterial are mainly as follows: electromechanical coupling coefficients ( $k_p$ ,  $k_{15}$ ,  $k_{33}$ ,  $k_{31}$ ,  $k_t$ ), piezoelectric modules ( $d_{31}$ ,  $d_{33}$ ,  $d_{15}$ ), longitudinal ultrasonic wave velocities ( $V_{1}^E$ ,  $V_{4}^D$ ,  $V_{3}^D$ ), relative permittivity ( $\varepsilon_{33}^T/\varepsilon_0$  and  $\varepsilon_{11}^T/\varepsilon_0$ ), electrical capacitance, and resonance/antiresonance frequencies.

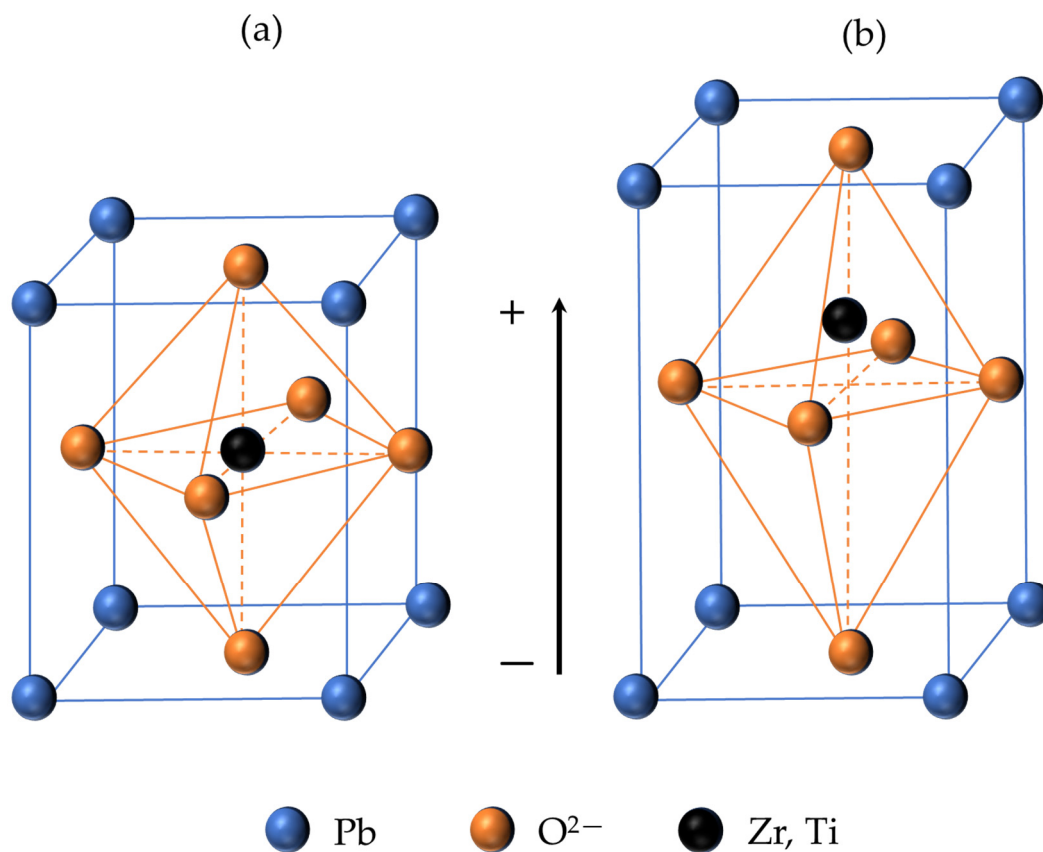


**Figure 1.** Behavior of the elementary cell of the PZT crystal above the Curie temperature (a) and below Curie temperature (b).

## 2.2. Piezoceramic Material Development and Investigation

PZT ceramics is a unique ferroelectric system, where “smeared” phase transitions can be realized in order to increase the morphotropic region [67]. Such systems are called ferroelectric relaxors [68]. By doping the PZT system with combined additives of lead magnoniobate, which in turn is a prominent representative of ferroelectric relaxors [69], as well as barium–strontium titanate, it was possible to obtain a new material: PKP-12 with a “smeared” phase transition. It has been established that the unique properties of relaxors are due to the formation and growth of nanoregions (nanodomains) in a crystal due to disorder in the environment of different ions located in crystallographically equivalent positions [70]. From the point of view of the use of these materials in the creation of multilayer actuators for wavefront correctors of the piezoactuator type, they make it possible to accurately control some properties of piezoceramics. For example, the value of the longitudinal piezoceramic coefficient  $d_{33}$  can be increased, which will lead to an increase in the displacement amplitude [65], however, this results in a decrease in the value of the Curie temperature.

The manufacturing of piezomaterials could be exploited two widely known ways: conventional [71] and colloidal-based techniques [72]. The main goal of both techniques is to obtain a homogeneous mixture of initial components—oxides or metals (Pb, Zr, Ti, etc.)

The main steps of these processes are shown in Figure 2 and it follows:

- For conventional ceramic technology, components are mixed in dry and wet grinding mills of a drum or planetary type.
- For colloidal-based method, the codeposition of components is carried out using a chemical reactor, centrifugation, and sputtering apparatuses.

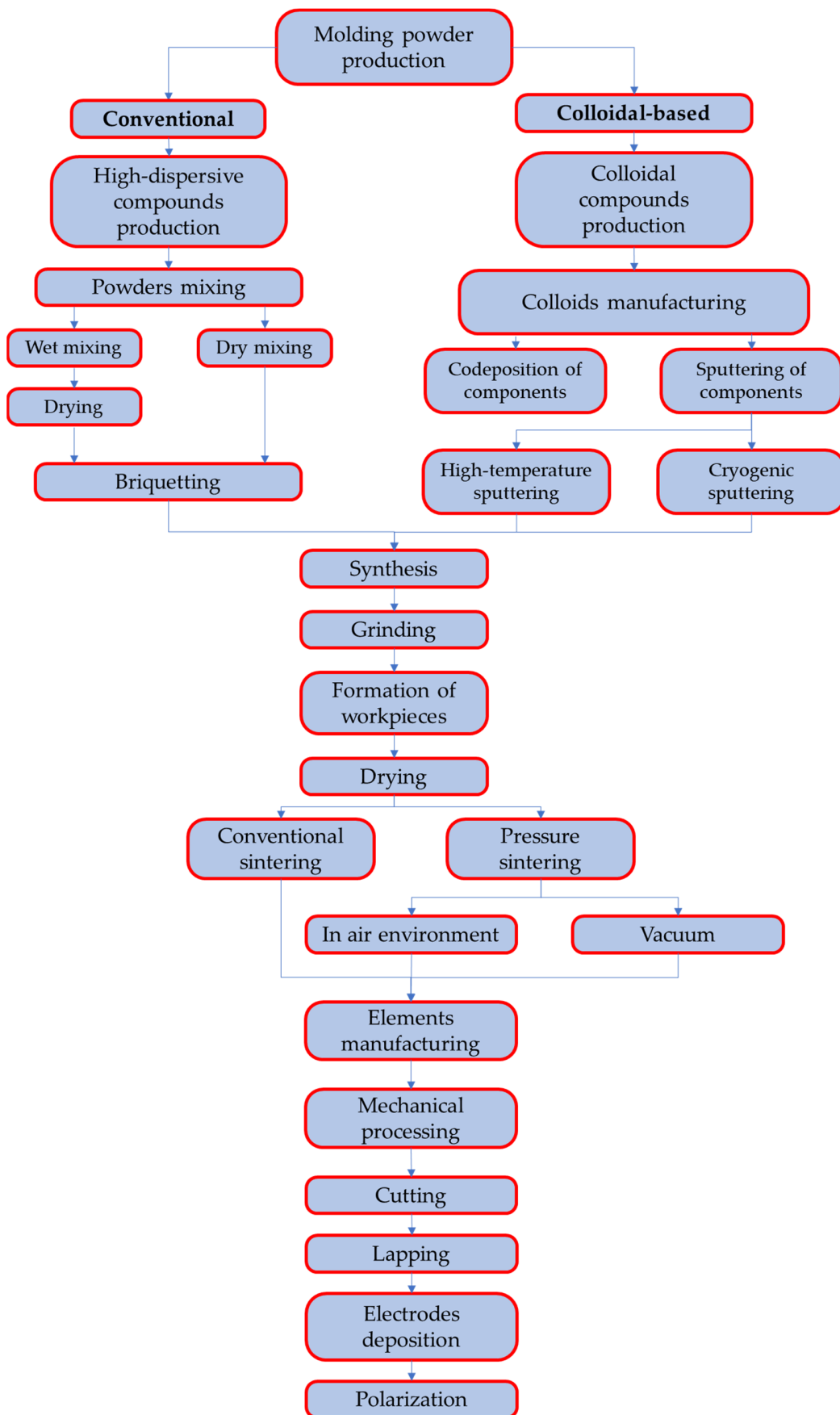


Figure 2. Scheme of piezoceramic material manufacturing process.

After obtaining a homogeneous mechanical mixture, the synthesis stage occurs. Synthesis with a method using solid-state reactions is uniform heating (with a constant rate of temperature rise) to a target temperature of 800–900 degrees, at which the synthesis reaction of a compound with necessary composition occurs.

The synthesized compound is re-grounded in a drum or planetary mill, dried to a residual moisture content of no more than 0.2 percent, after which the powder is ready for formation.

Formation is carried out by uniaxial isostatic hot pressing (with preliminary plasticization in a spray dryer, or the addition of a plasticizer). Such method of manufacturing of the piezomaterial allows for obtaining the samples with high density and reduced quantity of the inner hollows that decrease the probability of the electrical breakdown and increase the local deformation of the piezoelements [73].

To determine the main parameters of the material, a number of samples were made using conventional ceramic technology. Silver electrodes were deposited on the surface of all developed samples, except for elements with longitudinal polarization, by firing a silver-containing paste. When applying an electric field of 8 kV/cm for 10 min at a temperature of 120 °C, followed by direct natural cooling to room temperature, the samples were polarized in air.

To obtain samples with longitudinal polarization, the sintered block was divided into separate elements with electrodes deposited by chemical deposition [74].

Using dynamic measurement methods, the main electromechanical properties of the material were studied: relative permittivity, dielectric loss tangent  $\text{tg}\delta$ , electromechanical coupling coefficients, piezoelectric modules, ultrasonic waves velocities, mechanical quality factor  $Q_m$ , Poisson's ratio  $\delta p$ , and density  $\rho$ .

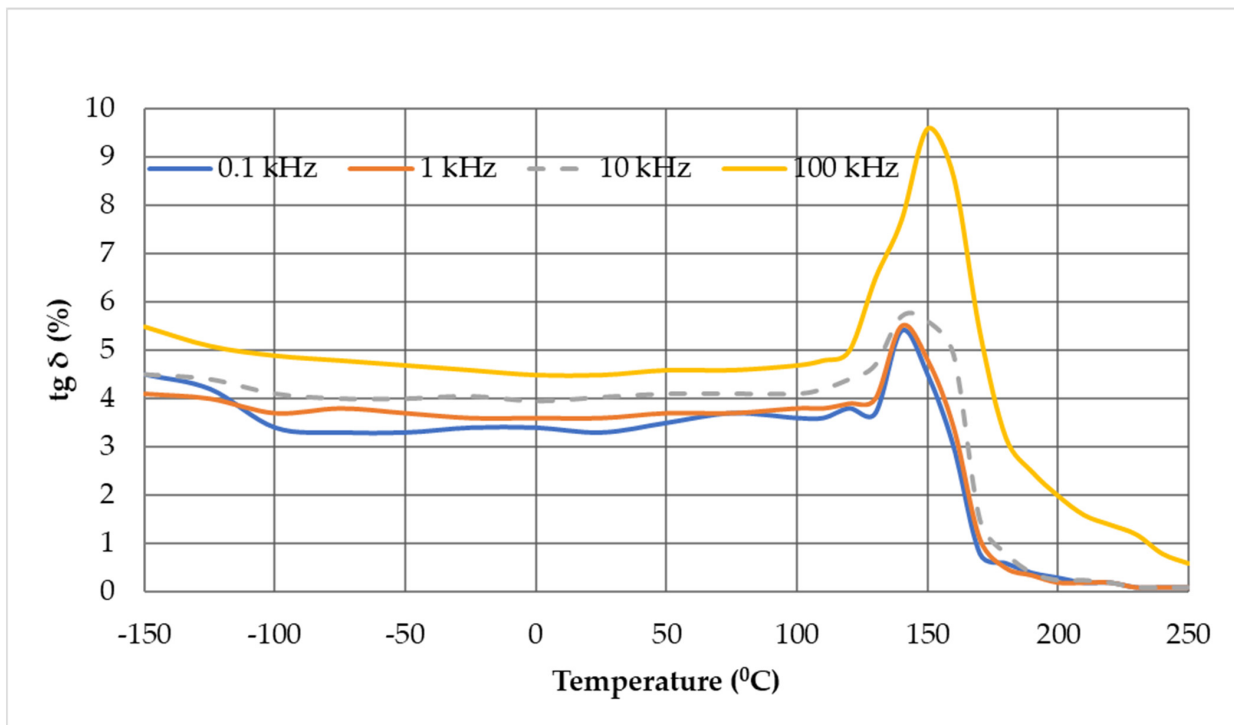
To obtain the electrical capacitance, resonance frequency, and antiresonance of the polarized piezoceramic samples, a Wayne Kerr Electronics WK 6510B precision impedance meter was used.

Figure 3 shows the temperature–frequency dependences of the relative permittivity ( $\epsilon' = \epsilon/\epsilon_0$ ) where  $\epsilon$  is the permittivity of the material,  $\epsilon_0$  is the dielectric constant, and  $\text{tg}\delta$  is the dielectric loss tangent of unpolarized ceramics at frequencies of 0.1, 1, 10, and 100 kHz.

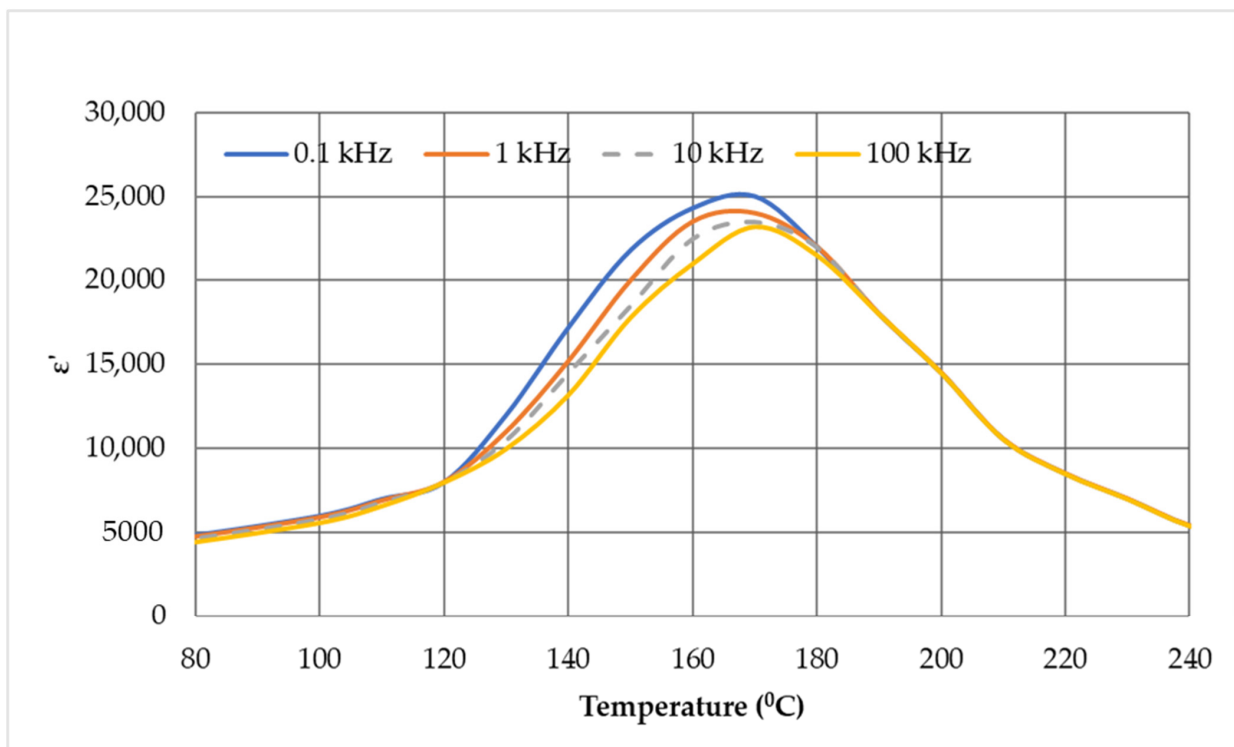
In the frequency range under consideration, a local temperature shift is clearly observed, where a maximum of the permittivity ( $T_m$ ) is observed as the frequency changes (Figure 3a), which is explicitly characteristic of relaxor ferroelectrics. In addition, the appearance of the dispersion effect is observed (situation when curves start to split at the various frequencies) at a temperature significantly below  $T_m$ . The maximum dispersion of the permittivity is observed at a temperature of about 130 °C. It should also be noted that the maximum of the dielectric loss tangent  $\text{tg}\delta$  ( $T$ ) has an asymmetric form at different temperatures (Figure 3b), which is also a distinctive feature of ferroelectric materials with a diffuse phase transition [75].

In our case, the possibility of the existence of a relaxor state in the material under study is also confirmed by the behavior of the elastic properties (Figure 4). So, from the temperature dependences of the piezomodulus  $d_{31}$  ( $T$ ) and the velocity of the longitudinal sound wave  $V_1^E$  ( $T$ ) in a polarized sample, it follows that the anomalies  $d_{31}$  ( $T$ ) in the form of a plateau-like maximum and  $V_1^E$  ( $T$ ) in the form of a very smeared minima are located significantly below  $T_m$ . In this case, a sharp drop in the values of  $d_{31}$  ( $T$ ) at  $T = 120$  °C and a jump in  $V_1^E$  ( $T$ ) at  $T \sim 110$  °C are associated with the onset of depolarization of the sample.

Taking into account that the temperature of the velocity minimum both in classical ferroelectrics and in relaxor ferroelectrics [76] corresponds to a phase transition, the temperature range from 20 to 150 °C can be the region of phase coexistence. In the material under study, this can first be the region of coexistence of the low-temperature rhombohedral phase R3c and the high-temperature rhombohedral phase R3m, and then the region of coexistence of the rhombohedral and tetragonal phases, and in the  $T_m$  region of the tetragonal and cubic phases.

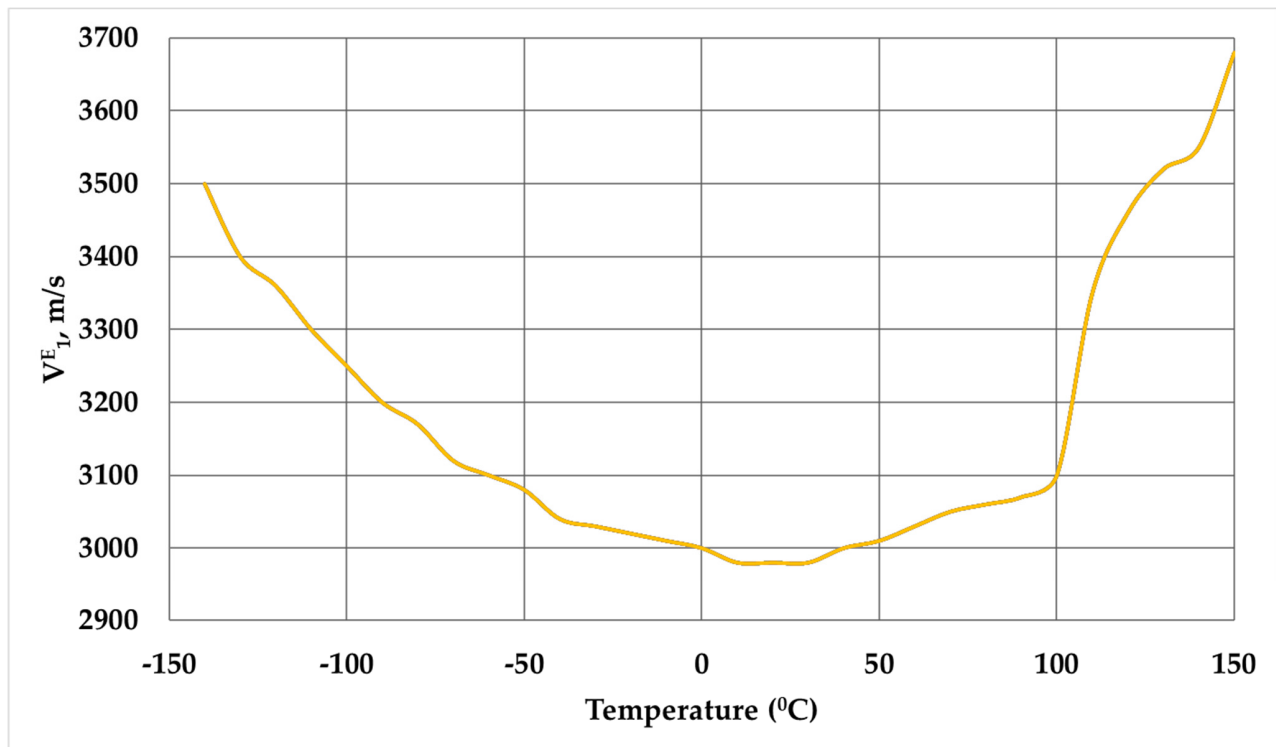


(a)

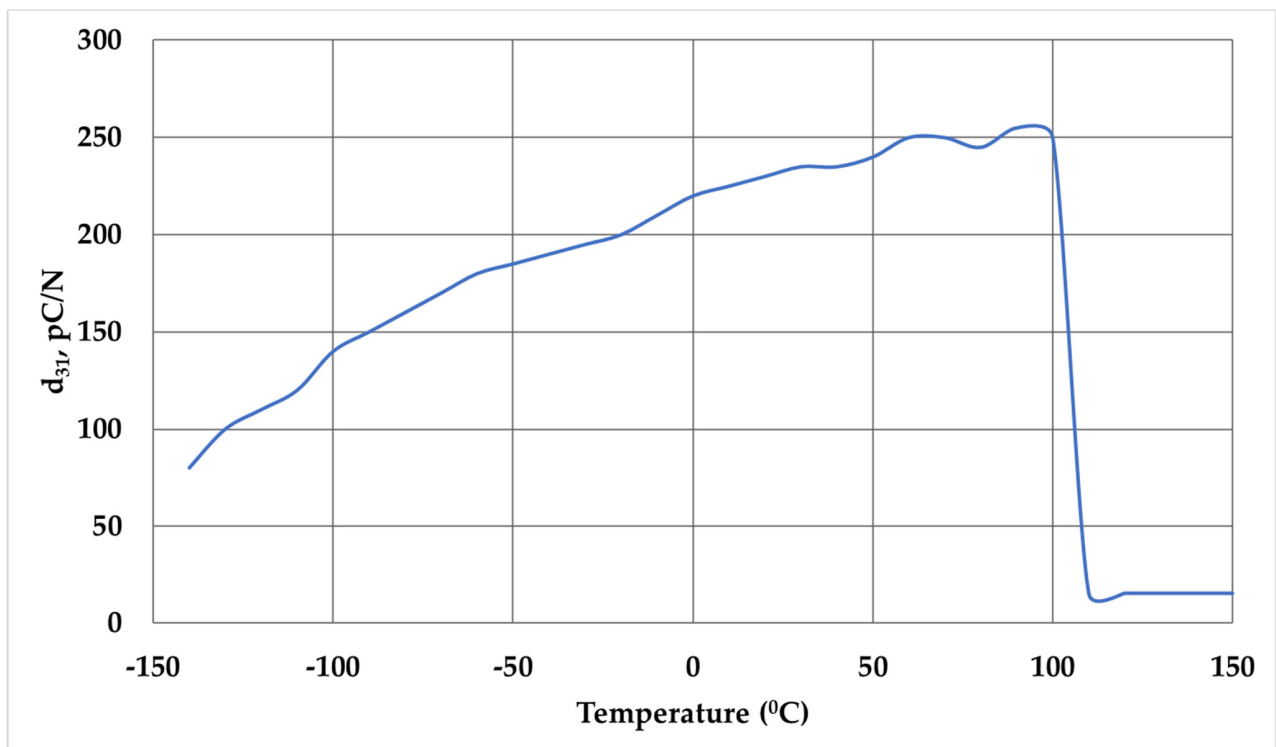


(b)

**Figure 3.** Dependence of the dielectric loss tangent  $tg \delta (T)$  (a) and the relative permittivity  $\epsilon' (T)$  (b), and of the unpolarized composition under study from the temperature and frequency.



(a)



(b)

**Figure 4.** Temperature dependence of the longitudinal ultrasonic waves velocity  $V_{1r}^{E_1}$  (T) (a) and piezomodulus  $d_{31r}$  (T) (b) of the developed material.

The behavior of the polarization of the resulting material was also studied depending on the applied external field. Figure 5 shows the dielectric hysteresis loop of the material under study, from which the value of the coercive field  $E_C \approx 4$  kV/cm was determined. The hysteresis loop is saturated and close in shape to the loop characteristic of ferrosoft ceramics.

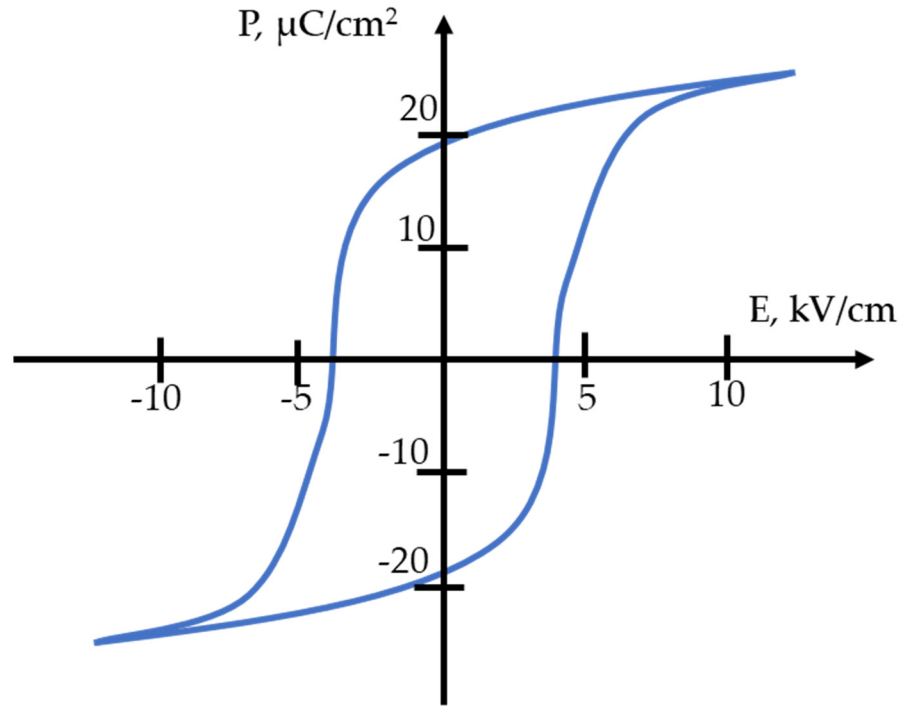


Figure 5. Hysteresis loop of the developed material.

The values of elastic compliance coefficients were also obtained to be used for the numerical modeling of piezoelements created on the basis of this material. Elastic compliance determines the amount of deformation that occurs under the influence of applied mechanical stress ( $\text{m}^2/\text{N}$ ).

$$\begin{pmatrix} S_{11}^E & S_{12}^E & S_{13}^E & 0 & 0 & 0 \\ S_{21}^E & S_{22}^E & S_{23}^E & 0 & 0 & 0 \\ S_{31}^E & S_{32}^E & S_{33}^E & 0 & 0 & 0 \\ 0 & 0 & 0 & S_{44}^E & 0 & 0 \\ 0 & 0 & 0 & 0 & S_{55}^E & 0 \\ 0 & 0 & 0 & 0 & 0 & S_{66}^E \end{pmatrix} = \begin{pmatrix} 1.76 & -0.59 & -0.81 & 0 & 0 & 0 \\ -0.59 & 1.76 & -0.81 & 0 & 0 & 0 \\ -0.81 & -0.81 & 1.88 & 0 & 0 & 0 \\ 0 & 0 & 0 & 4.47 & 0 & 0 \\ 0 & 0 & 0 & 0 & 4.47 & 0 \\ 0 & 0 & 0 & 0 & 0 & 4.71 \end{pmatrix} \cdot 10^{-11} \text{ m}^2/\text{N}$$

$$\begin{pmatrix} S_{11}^D & S_{12}^D & S_{13}^D & 0 & 0 & 0 \\ S_{21}^D & S_{22}^D & S_{23}^D & 0 & 0 & 0 \\ S_{31}^D & S_{32}^D & S_{33}^D & 0 & 0 & 0 \\ 0 & 0 & 0 & S_{44}^D & 0 & 0 \\ 0 & 0 & 0 & 0 & S_{55}^D & 0 \\ 0 & 0 & 0 & 0 & 0 & S_{66}^D \end{pmatrix} = \begin{pmatrix} 1.5 & -0.85 & -0.32 & 0 & 0 & 0 \\ -0.85 & 1.5 & -0.32 & 0 & 0 & 0 \\ -0.32 & -0.32 & 0.94 & 0 & 0 & 0 \\ 0 & 0 & 0 & 2.21 & 0 & 0 \\ 0 & 0 & 0 & 0 & 2.21 & 0 \\ 0 & 0 & 0 & 0 & 0 & 4.71 \end{pmatrix} \cdot 10^{-11} \text{ m}^2/\text{N}$$

Here,  $S_{ij}^E$  is the elastic compliance for stress in direction  $i$  (perpendicular to the direction in which the ceramic element is polarized) and accompanying strain in direction  $j$ , under a constant electric field (short circuit), and  $S_{ij}^D$  is the elastic compliance for stress in direction  $i$  (parallel to direction in which the ceramic element is polarized) and accompanying strain in direction  $j$ , under constant electric displacement (open circuit).

After that, the electrophysical characteristics of this composition were measured under standard conditions ( $T = 20 \pm 5$  °C). The measured data are presented in Table 1. Based on the data obtained, it can be established that the material under study has high values of dielectric permittivity, piezoelectric coefficients, and electromechanical coupling coefficients, which ultimately allow for the use of this material in the manufacturing of the devices for the tasks of actuator technology. Moreover, in comparison with piezomaterials from other manufacturers, this ceramic has a high value of the piezoelectric coefficient  $d_{33}$  and, at the same time, a low value of the dielectric loss tangent. A comparative analysis of the key parameters of widely known piezoelectric materials is shown in Table 2.

**Table 1.** Electrophysical characteristics of the developed material.

Parameter	Value
Curie temperature, $T_c$	160 °C
Relative permittivity $\epsilon_{33}^T/\epsilon_0$	4950
Relative permittivity $\epsilon_{11}^T/\epsilon_0$	4400
Dielectric loss tangent $\text{tg}\delta$ ,	1.5%
Electromechanical coupling coefficient $k_p$	0.66
Electromechanical coupling coefficient $k_{15}$	0.71
Electromechanical coupling coefficient $k_{33}$	0.70
Electromechanical coupling coefficient $k_{31}$	0.38
Electromechanical coupling coefficient $k_t$	0.53
Piezoelectrical coefficient $ d_{31} $	$325 \times 10^{-12}$ C/N
Piezoelectrical coefficient $d_{33}$	$660 \times 10^{-12}$ C/N
Piezoelectrical coefficient $d_{15}$	$940 \times 10^{-12}$ C/N
Longitudinal ultrasonic waves velocity $V_{E_1}$	$2770 \times 10^3$ m/s
Longitudinal ultrasonic waves velocity $V_{D_4}$	$2470 \times 10^3$ m/s
Longitudinal ultrasonic waves velocity $V_{D_3}$	$3700 \times 10^3$ m/s
Quality factor $Q_m$	60
Poisson ratio $\delta p$	0.34
Density $\rho$	7400 kg/m <sup>3</sup>

**Table 2.** Electrophysical characteristics of the developed material in comparison with piezoceramics available in the market.

Parameter	PKP-12	Sonox P51 (CeramTec AG, Plochingen, Germany)	OPT 5100 (Omega Piezo Technologies Inc., State College, PA, USA)	N-10 (Tokin, Shiroishi, Japan)
Relative permittivity $\epsilon_{33}^T/\epsilon_0$	4950	3100	3200	5440
Dielectric loss tangent $\text{tg}\delta$ , %	1.5	16	2	2
Piezoelectrical coefficient $ d_{31} $ ( $10^{-12}$ ), C/N	325	260	274	287
Piezoelectrical coefficient $d_{33}$ ( $10^{-12}$ ), C/N	660	640	550	635
Piezoelectrical coefficient $d_{15}$ ( $10^{-12}$ ), C/N	940	730	780	930

### 3. Results and Discussion

First of all, it is worth mentioning the principle of operation of the piezostack deformable mirror with modular design. In fact, this mirror is one of the modifications of a piezoactuator deformable mirror and consists of a relatively thin reflective plate, under which there are modules (cartridges) with individual multilayer piezoelectric stacks, assembled on a single pedestal and glued at one end to the rear side of the passive substrate, others—to a thick basement (Figure 6). Due to the inverse piezoelectric effect, when a control voltage is applied, the length of the piezostack changes. Since the piezoelectric actuator is rigidly fixed on the back side of the substrate, its elongation causes local deformation of

the reflecting surface. By applying a set of different voltages to such control elements, it is possible to form a desirable arbitrary shape of the surface of a deformable mirror.

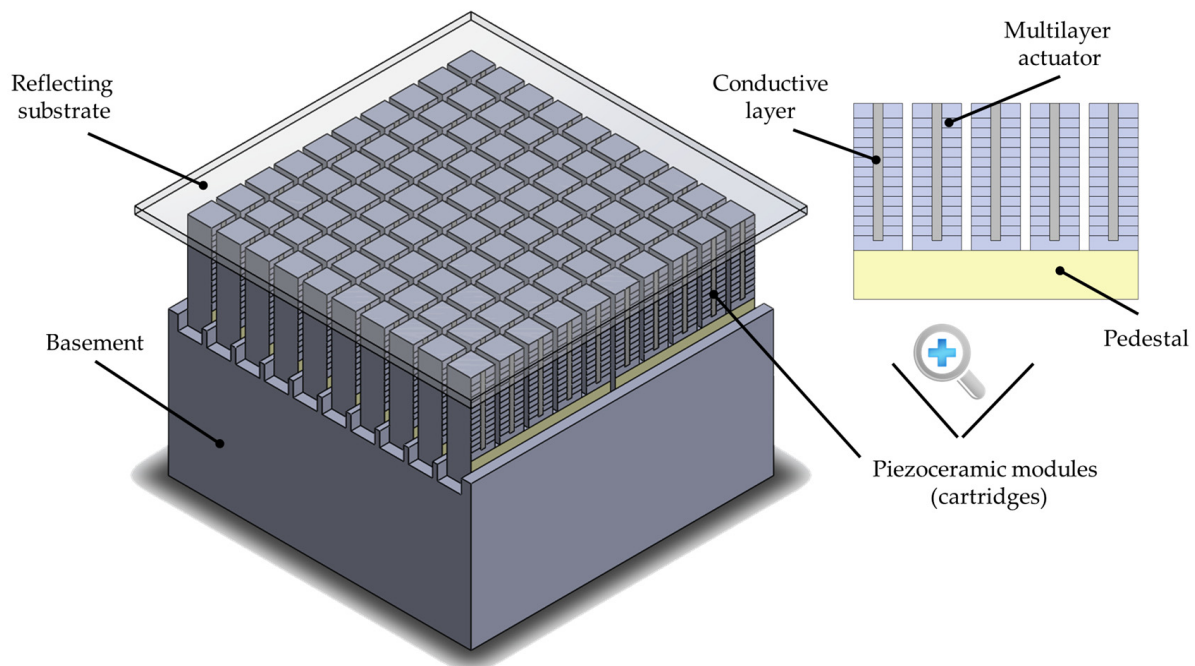


**Figure 6.** Scheme of the piezostack deformable mirror with modular design.

Based on the research data on the characteristics of piezomaterials presented in Section 2, multilayer modules with five separate control elements were made, although it is possible to create such modules with a large number of actuators, nevertheless, to ensure versatility and create deformable mirrors.

The production process of multi-element piezoceramic actuators is shown in Figure 7 and consists of the following steps:

First, a mixture (mixture of starting materials) of the PKP-12 piezoceramic material was prepared using the classical ceramic technology from metal oxides. The material was synthesized by the method of solid-phase reactions by firing the mixture in a muffle furnace at a temperature of 850 °C. After that, the mixture obtained was crushed into powder and granulated (1).

Then, the PKP-12 granular material was pressed into blocks, which were subsequently dried in an oven and fired in a muffle furnace at a temperature of 1230 °C (2). The sintered blocks were ground on all sides, then sawn into 5-mm-thick base elements (3) and 0.5-mm-thick active layers (4).

After that, a silver-containing paste was applied to the active piezoelectric layers, which was fired by soft annealing at a temperature of up to 700 °C. Next, part of the silver coating was removed in order to separate the tracks (5).

Prepared base elements sized 26 × 26 × 5.5 mm were assembled into a package with active layers (26 × 26 × 0.5 mm), after which the compression welding of the piezoceramic block (6) took place. The assembled and welded block was again subjected to mechanical processing (grinding of the end surfaces) (7), after which it was sawn into separate modules (8).

Further, the cut parts of the block were subjected to further sawing into separate actuators in such a way that the active layers were separated from each other by a gap of 1 mm, but remained rigidly fixed to the base element (9).

Each actuator of the resulting module was covered with a layer of silver-containing paste (burning method) in order to switch the electrodes of the active layers. Then, an SiF wire 0.4 mm thick was soldered to each current lead (Figure 8a).

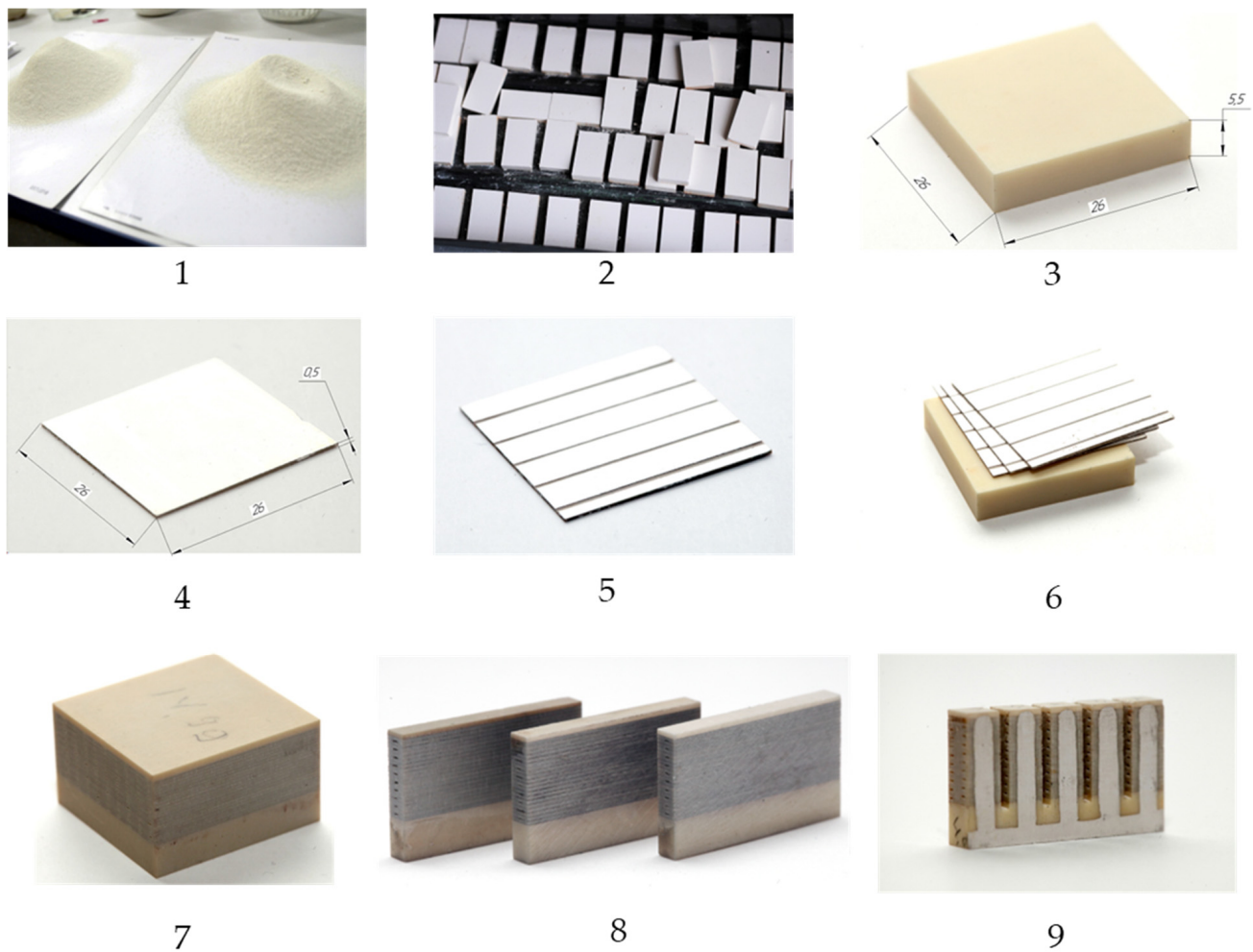


**Figure 7.** Scheme of the production cycle of the piezostack modules manufacturing.

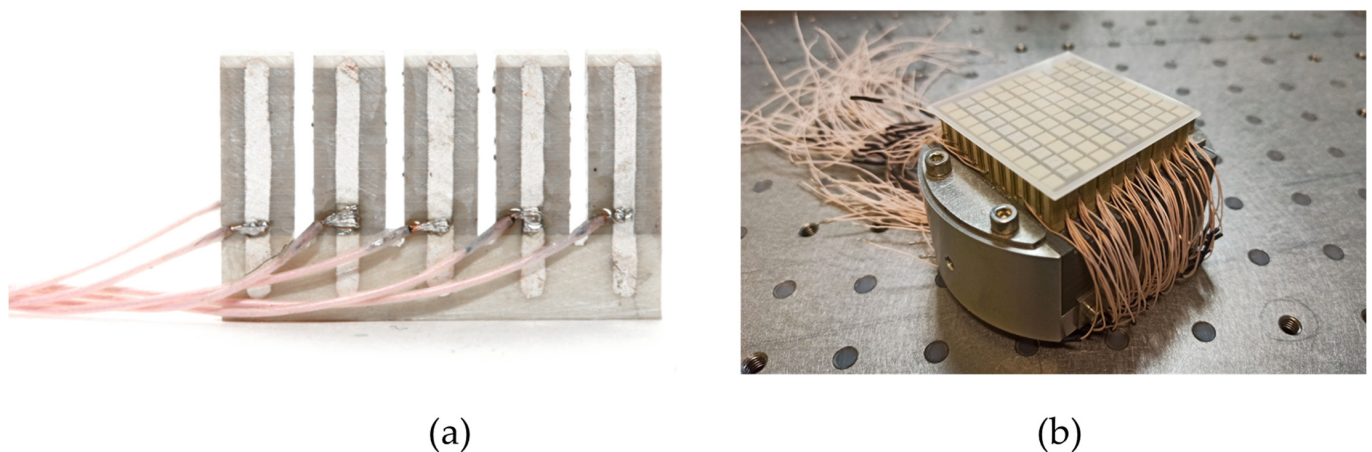


**Figure 8.** Piezostack deformable mirror with modular design: piezoceramic module with wiring (a), main view of the assembled deformable mirror (b).

Next, the process of polarization of the piezoceramics was carried out and the characteristics of individual actuators in the module were measured.

The obtained values are given in Table 3.

**Table 3.** Parameters of the manufactured piezomodules.

Parameter	Value
Capacitance of the single piezostack, $C_{\text{nom}}$	11–12 nF
Stroke under 300 V	4.1–4.3 $\mu$

It should be noted that the developed modules have a surface deformation amplitude of up to 4.3  $\mu\text{m}$ . Taking into account the fact that part of the range fails in overcoming the elastic forces due to the deformation of the reflecting substrate, in a piezoactuator deformable mirror, the local displacement will decrease by about 50% and will be  $>2 \mu\text{m}$ . Thus, these elements can be used in deformable mirrors of the piezoactuator type to correct for the phase fluctuations of the atmosphere of the Kolmogorov spectrum [77] on a path 1500 m long, a beam diameter of 250 mm, a structural constant of the refractive index of  $C_n^2 = 10^{-14} \text{m}^{-2/3}$ , and a coherence radius of 71 mm at a wavelength of 1064 nm [78–80].

In addition, when determining the speed of the system, one of the important indicators of the response speed will be the capacity of the control elements. Since the control element of actuator-type deformable mirrors is actually a piezoelectric capacitor, to control the charge and discharge of this capacitor, it is necessary to use the concept of an RC circuit, which shows the time during which the piezoceramic element has time to charge/discharge by 63% [81] of the initial voltage applied to change the length of the piezoplate or piezostack (the magnitude of the applied voltage does not affect the charge rate of the capacitor). Therefore, from the point of view of control theory, it is reasonable to use deformable mirrors with a lower value of the capacitance of the control elements. The values of electric capacitance for conventional mirrors are in the range up to 0.5  $\mu\text{F}$  [22–31].

In order to manufacture a piezostack deformable mirror with modular design with matrix of elements  $10 \times 10$ , we combined the cartridges on the rigid basement made of piezoceramic material. An aperture of the mirror of 50 x50 mm was chosen with square geometry of the control elements, however, such method of assembling allows for acquiring any net of the actuators and to scale the aperture of the deformable mirror. After assembly of the piezomodule part, the thin polished 1.5 mm glass substrate was glued on this part using the reference plate ( $\lambda/4$ ) to obtain a high quality of the initial surface of the mirror (Figure 8b).

After development of the modular piezostack deformable mirror, we investigated the key parameters of such a wavefront corrector–response function of actuators, and the amplitude-phase characteristic.

To measure the response functions of the control elements of the developed deformable mirror, the diagnostic setup based on the Shack–Hartmann wavefront sensor was used. The images of the mirror surface after applying the voltage of 300 V to different actuators are presented in Figure 9. As it could be seen from the presented data, the main surface deformation is of course concentrated in the range of the position of the actuators. At the same time, on the neighbor actuators one can also see the change in the mirror surface. This is due to the small (only 1 mm) distance between the actuators and also rather high thickness of the reflecting substrate (1.5 mm). In our case, the coupling coefficient was in the range of 60%. In addition, we expected the local stroke of the developed deformable mirror actuators be close to two microns, however, the measured data showed that the real local mirror displacement was just about one micron. Since the thickness of the individual layer of the actuator is 500  $\mu\text{m}$ , the control voltages could be increased up to 600 V (–200. . .+400 V) for the manufactured piezoceramic modules. Thus, the stroke should be close to the expected 2  $\mu\text{m}$ .

In addition, the first resonant frequency of the mirror was measured (Figure 10) by measuring amplitude-frequency and phased-frequency responses of the mirror. To measure the real value of this parameter we used the oscilloscope Tektronix DPO-2004B and a sine wave generator. The sine voltage with the frequency range from 0.1 to 8 kHz was applied to the actuator #45 (it could be applied to any piezostack). Due to the piezoelectric effect,

AC voltage was detected on the neighbor electrode #46 and was registered using the oscilloscope. The amplitude of the output signal was stable up to the frequency of 7.4 kHz, and the first resonance was found at the frequency of 7.5 kHz. Additionally, the temporal bandwidth of the deformable mirror could be described using the Bode Curve [82], which shows the use of such corrector in an adaptive optical system with frequency up to 7.4 kHz.

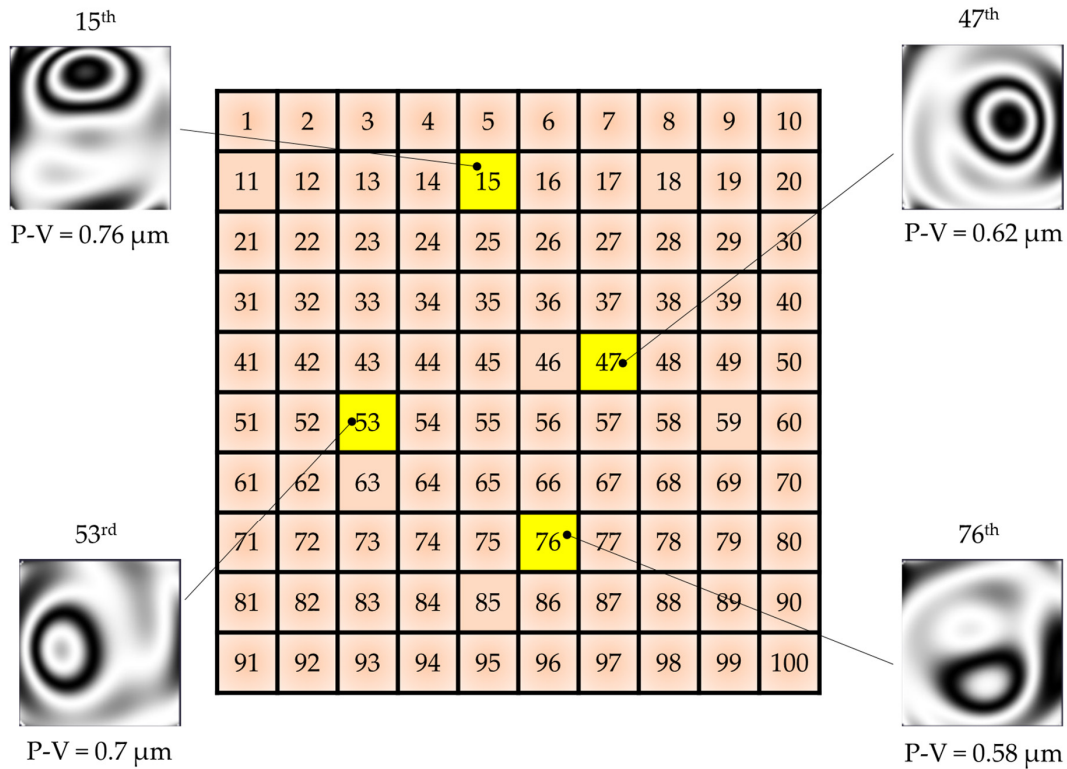


Figure 9. Response functions of the 15th, 47th, 53rd, and 76th actuators of the modular piezostack deformable mirror.

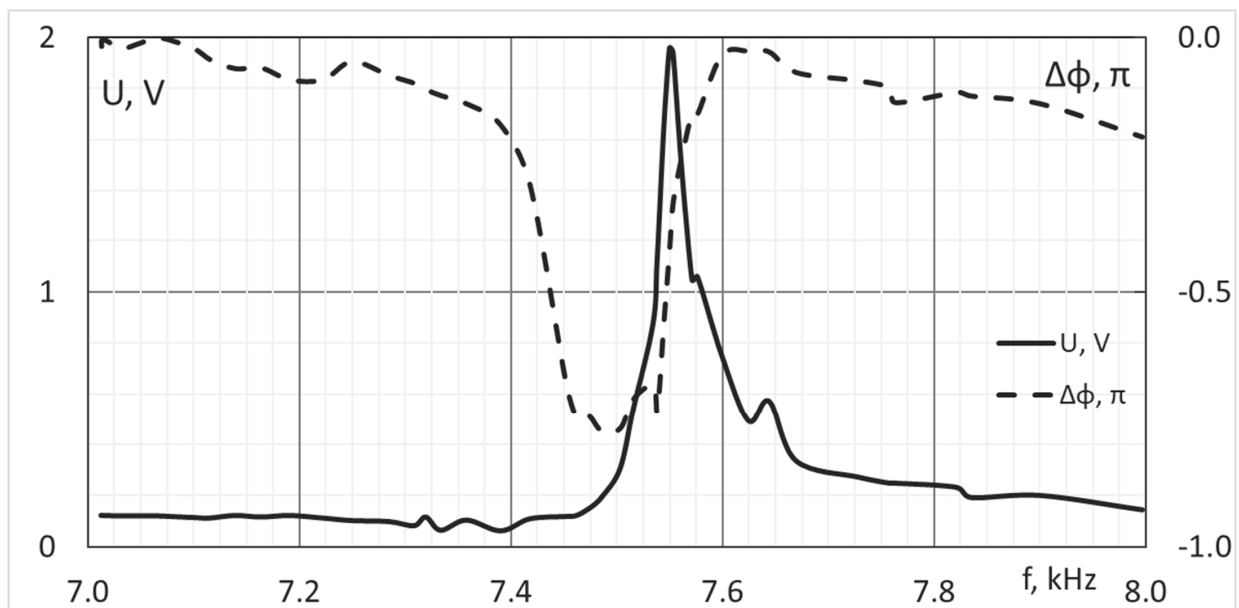


Figure 10. Amplitude-frequency (solid line) and phased-frequency (dashed line) responses of the developed piezostack deformable mirror.

#### 4. Conclusions

Based on the PZT ceramic, the PKP-12 piezoceramic material was produced. Key properties of the developed material such as electromechanical coupling coefficients ( $k_p$ ,  $k_{15}$ ,  $k_{33}$ ,  $k_{31}$ ,  $k_t$ ), piezoelectric modules ( $d_{31}$ ,  $d_{33}$ ,  $d_{15}$ ), longitudinal ultrasonic waves velocities ( $V^E_1$ ,  $V^D_4$ ,  $V^D_3$ ), relative permittivity ( $\epsilon^T_{33}/\epsilon_0$  and  $\epsilon^T_{11}/\epsilon_0$ ), electrical capacitance, resonance/antiresonance frequencies, dielectric loss tangent, mechanical quality factor, Poisson's ratio, and density were investigated. It was shown that in terms of elastic properties this material is very close to ferroelectric relaxors, having high compliance in a wide temperature range. In addition, the resulting material had a high value of the longitudinal piezoceramic coefficient of 660 pC/N and a low value of the dielectric loss tangent (no more than 1.5%). Therefore, such material could be applied for manufacturing of the multilayer actuators.

Based on the study of the electrophysical and mechanical parameters of the obtained materials, piezoceramic modules were fabricated with five multilayer actuators  $4 \times 4 \times 15$  mm. The capacitance of the individual actuator was 12 nF. The maximum displacement at a control voltage of 300 V was in the range of 4.1–4.3  $\mu\text{m}$ . The developed piezoelectric elements were used for the creation of the piezostack deformable mirror with modular design with the possibility of obtaining the required configuration of control elements by combining the developed piezoceramic modules.

**Author Contributions:** Conceptualization, V.T., V.S. and A.P.; methodology, A.P. and A.M.; validation, I.G., V.T. and V.S.; formal analysis, A.P. and A.K.; investigation, V.T.; resources, A.P. and A.K.; data curation, V.T. and I.G.; writing—original draft preparation, V.T., I.G. and A.M.; writing—review and editing, V.T., V.S. and A.P.; visualization, I.G. and A.M.; supervision, A.K. and A.P.; project administration, V.S. and A.P.; funding acquisition, V.S. All authors have read and agreed to the published version of the manuscript.

**Funding:** This research received no external funding.

**Data Availability Statement:** The data that supports the findings of this study are available from the corresponding author upon reasonable request.

**Conflicts of Interest:** The authors declare no conflict of interest.

#### References

1. Curie, J.; Curie, P. Développement par compression de l'électricité polaire dans les cristaux hémihédres à faces inclinées. *Bull. Société Minéralogique Fr.* **1880**, *3*, 90–93. [[CrossRef](#)]
2. Emamian, S.; Narakathu, B.; Chlahawi, A.; Atashbar, M. Fabrication and Characterization of Piezoelectric Paper Based Device for Touch and Force Sensing Applications. *Procedia Eng.* **2016**, *168*, 688–691. [[CrossRef](#)]
3. Sezer, N.; Koç, M. A comprehensive review on the state-of-the-art of piezoelectric energy harvesting. *Nano Energy* **2021**, *80*, 105567. [[CrossRef](#)]
4. Samarkin, V.; Sheldakova, J.; Toporovskiy, V.; Rukosuev, A.; Kudryashov, A. High-spatial resolution stacked-actuator deformable mirror for correction of atmospheric wavefront aberrations. *Appl. Opt.* **2021**, *60*, 6719–6724. [[CrossRef](#)] [[PubMed](#)]
5. Brown, C.; Kell, R.; Taylor, R.; Thomas, L. Piezoelectric Materials, A Review of Progress. *IRE Trans. Compon. Parts* **1962**, *9*, 193–211. [[CrossRef](#)]
6. Narkiewicz, J.P.; Done, G.T.S. Smart Internal Vibration Suppressor for a Helicopter BLADE—A Feasibility Study. *J. Sound Vib.* **1998**, *215*, 211–229. [[CrossRef](#)]
7. Veerasha, R.K.; Krishna Bhat, M.; Muralidhara, A. A novel piezoelectric motor design and its controller. *Mater. Today Proc.* **2023**, *in press*. [[CrossRef](#)]
8. Dong, W.; Chen, F.; Li, H.; Miao, Y.; Du, Z. A two-dimensional nano-positioner: Design, modelling and experiments. *Robot. Comput.-Integr. Manuf.* **2017**, *48*, 167–173. [[CrossRef](#)]
9. Chaudhary, H.; Khatoon, S.; Singh, R.; Pandey, A. Fast Steering Mirror for Optical Fine Pointing Applications: A Review Paper. In Proceedings of the 3rd International Innovative Applications of Computational Intelligence on Power, Energy and Controls with Their Impact on Humanity (CIPECH), Ghaziabad, India, 1–2 November 2018; pp. 1–5.
10. Zhou, J.; Yin, H.; Wang, Y. Research on the Structure and Dynamic Characteristics of a Fast-Steering Mirror. *Proc. SPIE* **2009**, *7281*, 72810J.
11. Spanner, K.; Koc, B. Piezoelectric Motors, an Overview. *Actuators* **2016**, *5*, 6. [[CrossRef](#)]

12. Pankaj, S.; Chandra, V.; Murat, R.; Kumar, V. Design and analysis of piezo actuated flexure guided nanopositioning stage. *Mater. Today Proc.* **2023**, *80*, 327–332. [[CrossRef](#)]
13. Khalate, A.A.; Bombois, X.; Scorletti, G.; Babuska, R.; Koekebakker, S.; de Zeeuw, W. A Waveform Design Method for a Piezo Inkjet Printhead Based on Robust Feedforward Control. *J. Microelectromech. Syst.* **2012**, *21*, 1365–1374. [[CrossRef](#)]
14. Toporovsky, V.; Kudryashov, A.; Skvortsov, A.; Rukosuev, A.; Samarkin, V.; Galaktionov, I. State-of-the-Art Technologies in Piezoelectric Deformable Mirror Design. *Photonics* **2022**, *9*, 321. [[CrossRef](#)]
15. Toporovskii, V.V.; Skvortsov, A.A.; Kudryashov, A.V.; Samarkin, V.V.; Sheldakova, Y.V.; Pshonkin, D.E. Flexible bimorphic mirror with high density of control electrodes for correcting wavefront aberrations. *J. Opt. Technol.* **2019**, *86*, 32–38. [[CrossRef](#)]
16. Fan, Z.; Dai, Y.; Guan, C.; Tie, G.; Qi, C.; Zhong, Y. Unimorph deformable mirror with an integrated strain feedback layer. *Appl. Opt.* **2018**, *57*, 6102–6109. [[CrossRef](#)] [[PubMed](#)]
17. Xue, Q.; Huang, L.; Yan, P.; Gong, M.L.; Qiu, Y.T.; Li, T.H.; Feng, Z.X.; Jin, G.F. Structure and closed-loop control of a novel compact deformable mirror for wavefront correction in a high-power laser system. *Laser Phys. Lett.* **2013**, *10*, 045301. [[CrossRef](#)]
18. Aghababayee, M.A.; Mosayebi, M.; Saghafifar, H. Calculation of the modified control matrix for a selected unimorph deformable mirror to compensate the piezoelectric hysteresis effect using the inverse Bouc–Wen model. *Appl. Opt.* **2022**, *61*, 2293–2305. [[CrossRef](#)] [[PubMed](#)]
19. Oya, S.; Bouvier, A.; Guyon, O.; Watanabe, M.; Hayano, Y.; Takami, H.; Iye, M.; Hattori, M.; Saito, Y.; Itoh, M.; et al. Performance of the deformable mirror for Subaru LGSAO. *Proc. SPIE* **2006**, *6272*, 62724S.
20. Cheriaux, G.; Rousseau, J.-P.; Burgy, F.; Sinquin, J.-C.; Lurçon, J.-M.; Guillemard, C. Monomorph large aperture adaptive optics for high peak-power femtosecond lasers. *Proc. SPIE* **2007**, *6584*, 658405.
21. Ma, J.; Li, B.; Chu, J. Characterization of a 61-element bulk-PZT thick film deformable mirror and generation of Zernike polynomials. *Proc. SPIE* **2010**, *7657*, 76570G.
22. Toporovskiy, V.; Kudryashov, A.; Samarkin, V.; Sheldakova, J.; Rukosuev, A. Water-cooled stacked-actuator deformable mirror for atmospheric applications. *Proc. SPIE* **2019**, *11135*, 111350A.
23. Toporovsky, V.; Kudryashov, A.; Samarkin, V.; Sheldakova, J.; Rukosuev, A. Wide aperture high resolution stacked-actuator deformable mirror for high power laser beam correction. *Proc. SPIE* **2019**, *10898*, 1089809.
24. Ahn, K.; Rhee, H.-G.; Yang, H.-S.; Kihm, H. CVD SiC deformable mirror with monolithic cooling channels. *Opt. Express* **2018**, *26*, 9724–9739. [[CrossRef](#)]
25. Włodarczyk, K.L.; Bryce, E.; Schwartz, N.; Strachan, M.; Hutson, D.; Maier, R.R.J.; Atkinson, D.; Beard, S.; Baillie, T.; Parr-Burman, P.; et al. Scalable stacked array piezoelectric deformable mirror for astronomy and laser processing applications. *Rev. Sci. Instrum.* **2014**, *85*, 024502. [[CrossRef](#)]
26. Fuschetto, A. Three-Actuator Deformable Water-Cooled Mirror. *Opt. Eng.* **1981**, *20*, 202310. [[CrossRef](#)]
27. Everson, J.H.; Aldrich, R.E.; Cone, M.; Kenemuth, J. Device Parameters and Optical Performance of a Stacked Actuator Deformable Mirror. *Proc. SPIE* **1980**, *0228*, 34–40.
28. Wirth, A.; Cavaco, J.; Bruno, T.; Ezzo, K.M. Deformable mirror technologies at AOA Xinetics. *Proc. SPIE* **2013**, *8780*, 87800M.
29. Sinquin, J.-C.; Lurçon, J.-M.; Guillemard, C. Deformable mirror technologies for astronomy at CILAS. *Proc. SPIE* **2008**, *7015*, 70150O.
30. Hickey, G.; Barbee, T.; Ealey, M.; Redding, D. Actuated hybrid mirrors for space telescopes. *Proc. SPIE* **2010**, *7731*, 773120.
31. Sun, L.; Zheng, Y.; Sun, C.; Huang, L. Simulational and experimental investigation on the actuator-corresponding high-frequency aberration of the piezoelectric stacked array deformable mirror. *Opt. Express* **2018**, *26*, 23613–23628. [[CrossRef](#)]
32. Patterson, K.; Pellegrino, S. Ultralightweight deformable mirrors. *Appl. Opt.* **2013**, *52*, 5327–5341.
33. Zhang, Y. Lightweight unimorph mirror using an optical replication method. *Opt. Eng.* **2019**, *58*, 085101. [[CrossRef](#)]
34. Abdulrazak, S.H.; Chistyakov, D.V.; Losev, S.N.; Mylnikov, V.Y.; Zadiranov, Y.M.; Deryagin, N.G.; Sokolovskii, G.S. Cancellation of side lobes in "droplet" Bessel beams generated with semiconductor laser. *Proc. ICLO* **2020**, *1*.
35. Abdulrazak, S.H.; Mylnikov, V.Y.; Chistyakov, D.V.; Losev, S.N.; Deryagin, N.G.; Dudelev, V.V.; Sokolovskii, G.S. Bessel beam generation from conically refracted laser diode radiation. *Proc. ICLO* **2022**, *1*.
36. Yu, X.; Todi, A.; Tang, H. Bessel beam generation using a segmented deformable mirror. *Appl. Opt.* **2018**, *57*, 4677–4682. [[CrossRef](#)] [[PubMed](#)]
37. Gong, L.; Ren, Y.-X.; Xue, G.-S.; Wang, Q.-C.; Zhou, J.-H.; Zhong, M.-C.; Wang, Z.-Q.; Li, Y.-M. Generation of nondiffracting Bessel beam using digital micromirror device. *Appl. Opt.* **2013**, *52*, 4566–4575. [[CrossRef](#)] [[PubMed](#)]
38. Tao, X.; Fernandez, B.; Azucena, O.; Fu, M.; Garcia, D.; Zuo, Y.; Chen, D.C.; Kubby, J. Adaptive optics confocal microscopy using direct wavefront sensing. *Opt. Lett.* **2011**, *36*, 1062–1064. [[CrossRef](#)] [[PubMed](#)]
39. Ma, X.-S.; Herbst, T.; Scheidl, T.; Wang, D.; Kropatschek, S.; Naylor, W.; Wittmann, B.; Mech, A.; Kofler, J.; Anisimova, E.; et al. Quantum teleportation over 143 kilometers using active feedforward. *Nature* **2012**, *489*, 269–273. [[CrossRef](#)]
40. Ke, X.; Wu, P. *Adaptive Optics Theory and Its Application in Optical Wireless Communication*; Springer: Singapore, 2022.
41. Laskin, A.; Juzumas, V.; Urniežius, A.; Laskin, V.; Šlekys, G.; Ostrun, A. Building beam shaping optics for micromachining. *Proc. SPIE* **2015**, *9346*, 934615.
42. Bergander, A.; Breguet, J.-M.; Schmitt, C.; Clavel, R. Micropositioners for microscopy applications based on the stick-slip effect. In Proceedings of the International Symposium on Micromechatronics and Human Science, Nagoya, Japan, 22–25 October 2000; pp. 213–216.

43. Mylnikov, V.Y.; Chistyakov, D.V.; Abdulrazak, S.H.; Deryagin, N.G.; Zadiranov, Y.M.; Losev, S.N.; Sokolovskii, G.S. Period of droplet quasi-Bessel beam generated with the round-tip axicon. *Tech. Phys. Lett.* **2022**, *48*, 48–51. [[CrossRef](#)]
44. Chistyakov, D.V.; Losev, S.N.; Abdulrazak, S.H.; Mylnikov, V.Y.; Kognovitskaya, E.A.; Zadiranov, Y.M.; Deryagin, N.G.; Dudelev, V.V.; Kuchinskii, V.I.; Sokolovskii, G., S. Generation of Droplet Quasi-Bessel Beams Using a Semiconductor Laser. *Opt. Spectrosc.* **2019**, *127*, 848–853. [[CrossRef](#)]
45. Lin, C.; Zheng, S.; Li, P.; Shen, Z.; Wang, S. Positioning Error Analysis and Control of a Piezo-Driven 6-DOF Micro-Positioner. *Micromachines* **2019**, *10*, 542. [[CrossRef](#)] [[PubMed](#)]
46. Schmerbauch, A.E.M.; Vasquez-Beltran, M.A.; Vakis, A.I.; Huisman, R.; Jayawardhana, B. Influence functions for a hysteretic deformable mirror with a high-density 2D array of actuators. *Appl. Opt.* **2020**, *59*, 8077–8088. [[CrossRef](#)] [[PubMed](#)]
47. Han, X.; Ma, J.; Bao, K.; Cui, Y.; Chu, J. Piezoelectric deformable mirror driven by unimorph actuator arrays on multi-spatial layers. *Opt. Express* **2023**, *31*, 13374–13383. [[CrossRef](#)] [[PubMed](#)]
48. Toporovsky, V.; Kudryashov, A.; Samarkin, V.; Sheldakova, J.; Rukosuev, A. Applicability of small size wavefront correctors to compensate for wavefront distortions in laser systems. *Proc. SPIE* **2020**, *11266*, 1126619.
49. Alaluf, D.; Bastaitis, R.; Wang, K.; Horodincea, M.; Martic, G.; Mokrani, B.; Preumont, A. Unimorph mirror for adaptive optics in space telescopes. *Appl. Opt.* **2018**, *57*, 3629–3638. [[CrossRef](#)] [[PubMed](#)]
50. Ma, J.; Liu, Y.; He, T.; Li, B.; Chu, J. Double drive modes unimorph deformable mirror for low-cost adaptive optics. *Appl. Opt.* **2011**, *50*, 5647–5654. [[CrossRef](#)] [[PubMed](#)]
51. Wilcox, C.C.; Andrews, J.R.; Restaino, S.R.; Teare, S.W.; Payne, D.M.; Krishna, S. Analysis of a combined tip-tilt and deformable mirror. *Opt. Lett.* **2006**, *31*, 679–681. [[CrossRef](#)] [[PubMed](#)]
52. Madec, P.-Y. Overview of deformable mirror technologies for adaptive optics and astronomy. *Proc. SPIE* **2012**, *8447*, 844705.
53. Xu, W.; King, T.G. Mechanical amplifier design for piezo-actuator applications. In Proceedings of the IEE Colloquium on Innovative Actuators for Mechatronic Systems, London, UK, 18 October 1995; pp. 1–5.
54. Qi, K.; Xiang, Y.; Fang, C.; Zhang, Y.; Yu, C. Analysis of the displacement amplification ratio of bridge-type mechanism. *Mech. Mach. Theory* **2015**, *87*, 45–56. [[CrossRef](#)]
55. Yang, X.F.; Li, W.; Liu, Y.F. Displacement Amplification Analysis for Parallel Four-Bar Mechanism. *AMM* **2012**, *160*, 229–233. [[CrossRef](#)]
56. Tian, Y.; Shirinzadeh, B.; Zhang, D.; Alici, G. Development and dynamic modelling of a flexure-based Scott-Russell mechanism for nano-manipulation. *Mech. Syst. Signal Process.* **2009**, *23*, 957–978. [[CrossRef](#)]
57. Shamsipour, N.; Mobashery, A.; Moradi, M. Bit error rate reduction of optical communication by means of Tip/Tilt correction. *Opt. Commun.* **2019**, *429*, 152–157. [[CrossRef](#)]
58. Verpoort, S.; Rausch, P.; Wittrock, U. Characterization of a miniaturized unimorph deformable mirror for high power CW-solid state lasers. *Proc. SPIE* **2012**, *8253*, 825309.
59. Rausch, P.; Verpoort, S.; Wittrock, U. Unimorph deformable mirror for space telescopes: Design and manufacturing. *Opt. Express* **2015**, *23*, 19469–19477. [[CrossRef](#)] [[PubMed](#)]
60. Zhu, Z.; Li, Y.; Chen, J.; Ma, J.; Chu, J. Development of a unimorph deformable mirror with water cooling. *Opt. Express* **2017**, *25*, 29916–29926. [[CrossRef](#)] [[PubMed](#)]
61. Toporovsky, V.; Samarkin, V.; Sheldakova, J.; Rukosuev, A.; Kudryashov, A. Water-cooled stacked-actuator flexible mirror for high-power laser beam correction. *Opt. Laser Technol.* **2021**, *144*, 107427. [[CrossRef](#)]
62. Feinleib, J.; Lipson, S.G.; Cone, P.E. Monolithic piezoelectric mirror for wavefront correction. *Appl. Phys. Lett.* **1974**, *25*, 311–313. [[CrossRef](#)]
63. Aggogeri, F. Design of piezo-based AVC system for machine tool applications. *Mech. Syst. Signal Process.* **2013**, *36*, 53–65. [[CrossRef](#)]
64. Kosevich, A. *The Crystal Lattice: Phonons, Solitons, Dislocations, Superlattices*, 2nd ed.; Revised and Updated Edition; Wiley-VCH: New York, NY, USA, 2005.
65. Rupitsch, S.J. *Piezoelectric Sensors and Actuators: Fundamentals and Applications*, 1st ed.; Springer: Berlin/Heidelberg, Germany, 2018.
66. Anjana, J.; Prashanth, K.P.; Sharma, A.; Jain, A.; Rashmi, P.N. Dielectric and piezoelectric properties of PVDF/PZT composites: A review. *Polym. Eng. Sci.* **2015**, *55*, 1589–1616.
67. Lushnikov, S.G.; Fedoseev, A.I.; Gvasaliya, S.N.; Kojima, S. Anomalous dispersion of the elastic constants at the phase transformation of the  $\text{PbMg}_{1/3}\text{Nb}_{2/3}\text{O}_3$  relaxor ferroelectric. *Phys. Rev. B* **2008**, *77*, 104122. [[CrossRef](#)]
68. Viehland, D.; Jang, S.J.; Cross, L.E.; Wuttig, M. Deviation from Curie-Weiss behavior in relaxor ferroelectrics. *Phys. Rev. B* **1992**, *46*, 8003. [[CrossRef](#)] [[PubMed](#)]
69. Hao, J.; Li, W.; Zhai, J.; Chen, H. Progress in high-strain perovskite piezoelectric ceramics. *Mater. Sci. Eng. R Rep.* **2019**, *135*, 1–57. [[CrossRef](#)]
70. Bokov, A.A.; Ye, Z.-G. Recent progress in relaxor ferroelectrics with perovskite structure. *J. Mater. Sci.* **2006**, *41*, 31. [[CrossRef](#)]
71. Klocke, F. Modern approaches for the production of ceramic components. *J. Eur. Ceram. Soc.* **1997**, *17*, 457–465. [[CrossRef](#)]
72. Lewis, J.A. Colloidal Processing of Ceramics. *J. Am. Ceram. Soc.* **2000**, *83*, 2341–2359. [[CrossRef](#)]
73. Li, Z.; Sun, H.; Liu, X.; Sui, H.; Guo, H. High performance lead-free  $\text{Na}_0.5\text{K}_{0.5}\text{NbO}_3$  piezoelectric ceramics obtained via oscillatory hot-pressing. *Ceram. Int.* **2020**, *46*, 11617–11621. [[CrossRef](#)]
74. Ilyin, V.A. *Metallization of Dielectrics*; Mashinostroenie: Leningrad, Russia, 1977.

75. Isupov, V.A. Diffuse ferroelectric phase transition and PLZT ceramics. *Ferroelectrics* **1992**, *131*, 41–48. [[CrossRef](#)]
76. Smirnova, E.; Sotnikov, A.; Zaitseva, N.; Schmidt, H.; Weihnacht, M. Acoustic properties of multiferroic  $\text{PbFe}_{1/2}\text{Ta}_{1/2}\text{O}_3$ . *Phys. Lett. A* **2010**, *374*, 4256–4259. [[CrossRef](#)]
77. Galaktionov, I.; Sheldakova, J.; Samarkin, V.; Toporovsky, V.; Kudryashov, A. Atmospheric Turbulence with Kolmogorov Spectra: Software Simulation, Real-Time Reconstruction and Compensation by Means of Adaptive Optical System with Bimorph and Stacked-Actuator Deformable Mirrors. *Photonics* **2023**, *10*, 1147. [[CrossRef](#)]
78. Rukosuev, A.; Nikitin, A.; Toporovsky, V.; Sheldakova, J.; Kudryashov, A. Real-Time correction of a laser beam wavefront distorted by an artificial turbulent heated airflow. *Photonics* **2022**, *9*, 351. [[CrossRef](#)]
79. Rukosuev, A.; Nikitin, A.; Belousov, V.; Sheldakova, J.; Toporovsky, V.; Kudryashov, A. Expansion of the laser beam wavefront in terms of Zernike polynomials in the problem of turbulence testing. *Appl. Sci.* **2021**, *11*, 12112. [[CrossRef](#)]
80. Toporovsky, V.; Samarkin, V.; Kudryashov, A.; Galaktionov, I. Bimorph deformable mirror parameters optimization in atmospheric applications. *Proc. SPIE* **2022**, *12218*, 1221806.
81. Mada Sanjaya, W.S.; Anggraeni, D.; Sambas, A.; Denya, R. Numerical Method and Laboratory Experiment of RC Circuit using Raspberry Pi Microprocessor and Python Interface. *J. Phys. Conf. Ser.* **2018**, *1090*, 1. [[CrossRef](#)]
82. Samarkin, V.; Alexandrov, A.; Galaktionov, I.; Kudryashov, A.; Nikitin, A.; Rukosuev, A.; Toporovsky, V.; Sheldakova, J. Wide-Aperture Bimorph Deformable Mirror for Beam Focusing in 4.2 PW Ti:Sa Laser. *Appl. Sci.* **2022**, *12*, 1144. [[CrossRef](#)]

**Disclaimer/Publisher’s Note:** The statements, opinions and data contained in all publications are solely those of the individual author(s) and contributor(s) and not of MDPI and/or the editor(s). MDPI and/or the editor(s) disclaim responsibility for any injury to people or property resulting from any ideas, methods, instructions or products referred to in the content.